# Revealing the Mechanism behind the Catastrophic Failure of n-i-p Type Perovskite Solar Cells under Operating Conditions and How to Suppress It

*Changzeng Ding, Li Yin, Lianping Zhang, Rong Huang, Shizhao Fan, Qun Luo, Jian Lin, Fangsen Li, Chun Zhao, Ronald Österbacka,\* and Chang-Qi Ma\**

The n-i-p type perovskite solar cells suffer unpredictable catastrophic failure under operation, which is a barrier for their commercialization. The fluorescence enhancement at Ag electrode edge and performance recovery after cutting the Ag electrode edge off prove that the shunting position is mainly located at the edge of device. Surface morphology and elemental analyses prove the corrosion of the Ag electrode and the diffusion of $Ag^+$ ions on the edge for aged cells. Moreover, much condensed and larger Ag clusters are formed on the $MoO_3$ layer. Such a contrast is also observed while comparing the central and the edge of the Ag/Spiro-OMeTAD film. Hence, the catastrophic failure mechanism can be concluded as photon-induced decomposition of the perovskite film and release reactive iodide species, which diffuse and react with the loose Ag clusters on the edge of the cell. The corrosion of the Ag electrode and the migration of $Ag^+$ ions into Spiro-OMeTAD and perovskite films lead to the forming of conducting filament that shunts the cell. The more condensed Ag cluster on the $MoO_3$ surface as well as the blocking of holes within the Spiro-OMeTAD/$MoO_3$ interface successfully prevent the oxidation of Ag electrode and suppress the catastrophic failure.

## 1. Introduction

Hybrid organic–inorganic perovskites (HOIPs) have attracted wide attention for use in photovoltaics owing to their excellent optical and electrical properties.[1–3] In 2009, HOIPs were first applied in solar cells, and low efficiency of 3.8% was reported.[4] After more than 10 years of development, perovskite solar cells (PSCs) have emerged as a new generation of photovoltage (PV) technology with a performance boost to 25.5%.[5] Recently, device stability has emerged as an important obstacle for commercial applications.[6–10] There are various degradation pathways for PSCs, including: a) the decomposition of perovskite materials,[7] b) degradation caused by interfaces reaction,[8] c) corrosion of the metal electrode,[11] and d) ions migration in the whole device.[12] It is known that the reaction of HOIPs with water and oxygen molecules changes the crystalline structure and/or decomposition of the perovskite films.[13–15] However, this issue can be addressed by strict encapsulation and the stability of devices was significantly improved after proper packaging.[16,17] During operational stability tests, light and bias can simultaneously affect the stability of PSCs.[18–20] The ion migration induced by electrical bias and halide segregation in the bulk perovskite layer during illumination also causes instability of PSCs.[21,22] In

C. Ding, Dr. Q. Luo, Prof. C.-Q. Ma
School of Nano-Tech and Nano-Bionics
University of Science and Technology of China
398 Jinzhai Road, Hefei 230026, P. R. China
E-mail: cqma2011@sinano.ac.cn
C. Ding, L. Zhang, Dr. Q. Luo, Dr. J. Lin, Prof. C.-Q. Ma
Printable Electronic Research Center
Suzhou Institute of Nano-Tec and Nano-Bionics
Chinese Academy of Sciences (CAS)
398 Ruoshui Road, SEID, SIP, Suzhou 215123, P. R. China
L. Yin, Dr. C. Zhao
School of Science
School of Advanced Technology
Xi'an Jiaotong-Liverpool University
Suzhou 215123, China

The ORCID identification number(s) for the author(s) of this article
can be found under https://doi.org/10.1002/adfm.202103820.

Dr. R. Huang, Dr. F. Li
Vacuum Interconnected Nanotech Workstation
Suzhou Institute of Nano-Tec and Nano-Bionics
Chinese Academy of Sciences (CAS)
398 Ruoshui Road, SEID, SIP, Suzhou 215123, P. R. China
Prof. S. Fan
Nano-Devices and Materials Division
Suzhou Institute of Nano-Tech and Nano-Bionics
Chinese Academy of Sciences (CAS)
398 Ruoshui Road, SEID, SIP, Suzhou 215123, P. R. China
Prof. R. Österbacka
Physics and Center for Functional Materials
Faculty of Science and Technology
Åbo Akademi University
Porthaninkatu 3, Turku 20500, Finland
E-mail: Ronald.Osterbacka@abo.fi

**ADVANCED**
**SCIENCE NEWS**
www.advancedsciencenews.com

**ADVANCED**
**FUNCTIONAL**
**MATERIALS**
www.afm-journal.de

addition to the instability of perovskite materials, decompositions of the interfacial layer and/or electrode are also considered important reasons for the performance deterioration of PSCs. For example, light illumination on the $TiO_2$/PSCs, especially under Ultraviolet (UV) light exposure, leads to the formation of reactive superoxide species at the $TiO_2$/perovskite interface, which oxidizes the perovskite materials and cause performance decay.[23] By passivating the $TiO_2$ layer with CsBr, the photocatalytic activity of $TiO_2$ was significantly reduced, and the PSC showed improved stability even under UV exposure.[23] Similarly, Christians et al. reported that replacing the $TiO_2$ layer with $SnO_2$ was also able to improve device stability. With this, operational stability over 1000 h was achieved even under full-spectrum irradiation.[24] The metal electrode corrosion-induced device degradation was revealed as another important reason for PSCs' limited lifetime. The HI,[6] $I_2$,[7] and methyl-ammonium polyiodides ($MAI_x$) ($x = 3,5,7$),[25] originated from the decomposition of the perovskite layer, can react with commonly used metal electrodes, such as Ag and Au. Studies have demonstrated that Ag or Au can be corroded to form AgI[26–28] or iodine-gold complex[25,29] at the electrode interface. Several interface engineering strategies have been adopted to fabricate stable PSCs by introducing extra diffusion barriers between perovskite and metal electrodes, such as oxo-functionalized graphene/dodecylamine,[30] methylammonium bromide,[31] carbon quantum dots,[32] and cross-linked polymer.[33] The introduction of these barrier layers can effectively slow down the corrosion of electrodes and prolong the stability of the devices.

In addition to the gradual degradation processes, unpredictable catastrophic failures are frequently found in electronic devices,[34] limiting their ultimate useful lifetime. The potential-induced degradation in photovoltaic modules could potentially cause the catastrophic failures of silicon solar cells and modules, making it difficult to predict the overall lifetime.[35,36] Although in most literature reports, the PSCs typically depicted an exponential decay process, we show in this paper that n-i-p type PSCs also undergo unpredicted catastrophic failures within tens to a hundred hours under light illumination. By systematical investigation on the aged cell, we prove that the undesired shunting of the cell mainly occurs at the edge of the Ag electrode, which is originally from the corrosion of Ag electrode by the photon generated reactive iodinated species. With these results, detailed failure mechanisms and effective method to suppress the catastrophic failure in PSCs are suggested.

## 2. Result and Discussion

### 2.1. Performance Decay Dynamics of the Cells

The n-i-p PSCs studied in this work have a structure of Glass/ITO/$SnO_2$/$K_{0.035}Cs_{0.05}(FA_{0.83}MA_{0.17})_{0.95}Pb(I_{0.83}Br_{0.17})_3$/Spiro-OMeTAD (LiTFSI:$t$-BP)/Ag (inset in **Figure 1**a), where tri-cations CsFAMA based perovskite film doped with $K^+$ was used as the photoactive layer,[37] LiTFSI:$t$-BP doped Spiro-OMeTAD and $SnO_2$ were used as the hole and electron transporting layers, respectively.[38,39] The device fabrication processes were optimized according to the literature[37] and the averaged power conversion efficiencies (PCE) of these cells were measured to be 18.95 ± 0.31% with a short-circuit current ($J_{SC}$) of 23.07 ± 0.16 mA cm$^{-2}$, an open-circuit voltage ($V_{OC}$) of 1.08 ± 0.01 V, and a fill factor (FF) of 0.76 ± 0.01. The photovoltaic performance data are shown in Table S1, Supporting Information, which are comparable to that reported in the literature.[40,41] The cells were then aged inside a $N_2$ glove box under white LED light illumination (see Experimental Section for more details). The cell performance decay dynamics were recorded by checking the current-voltage ($J$–$V$) characteristics of the cells every 1 h with a sweeping range of −0.05–1.2 V. To better simulate the decay behaviors of the cells under real working condition, an external load was attached to individual cell to match the maximum power point during the $J$–$V$ sweeping break, in accordance to the requirement of IEC TS 62876-2-1:2018.[42] Figure 1a shows the evolution of $V_{OC}$, $J_{SC}$, FF, and PCE of a typical cell under operation for 130 h (see Figure S1, Supporting Information for the decay curves of 8 individual cells). The cell showed two distinct stages of decay dynamics, a slow exponential decay stage with performance loss of 20% over 98 h, a typical "burn-in" degradation originated from ion migration within the cell,[43] and a sudden drastic failure process occurring within a few hours. Comparison of failure $J$–$V$ characteristics showed that performance loss was mainly due to $V_{OC}$ and FF loss, while high $J_{SC}$ can still be achieved (Figure 1b). An almost linear $J$–$V$ character was measured for the failed
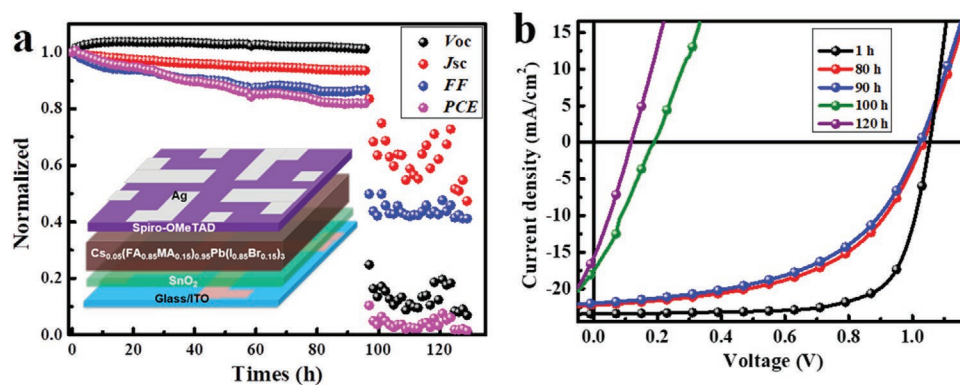


**Figure 1.** a) Decay dynamics of typical cells under continuous illumination and inset shows the architecture of perovskite solar cells adopted in this study. b) The $J$–$V$ curves of solar cells during operational stability test with different times.
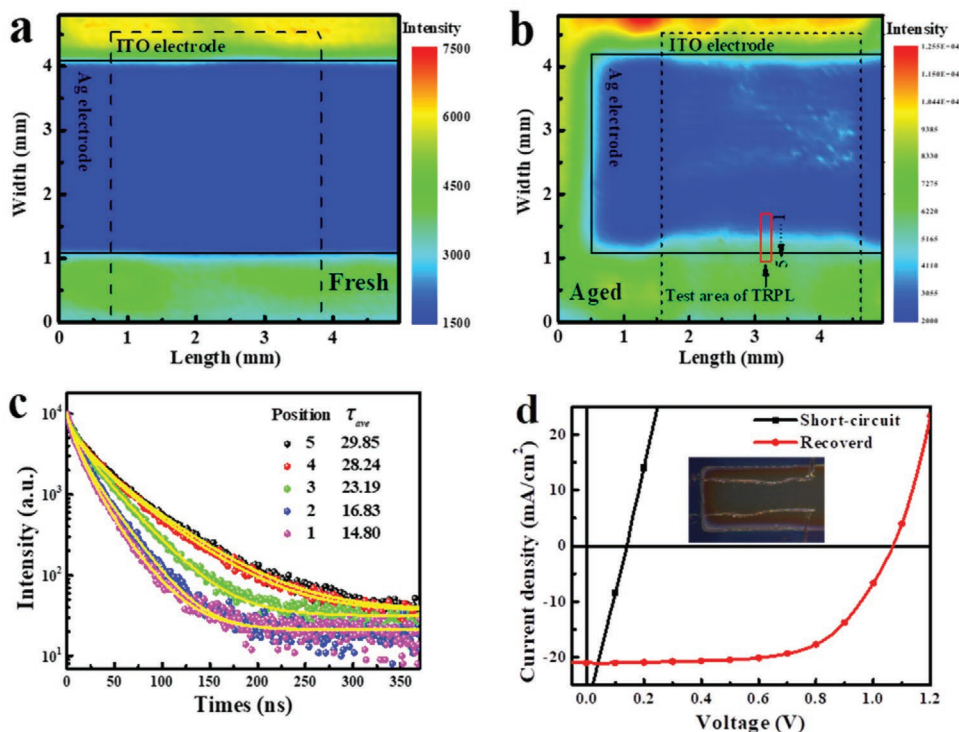
**Figure 2.** The photoluminescence (PL) mapping of a cell a) before and b) after aging, the excitation wavelength ($\lambda_{ex}$) is 532 nm and emission maximum wavelength ($\lambda_{em}^{max}$) is 760 nm. c) TRPL fluorescence decay curves of the perovskite films at different positions shown in (b). d) I–V curves of an aged cell and after cut-off the edges (see inset for the photo). Note the $y$ axis is in current intensity measure directly, since the cell area after cutting the edge away is difficult to measure.

cell, indicating that the catastrophic failure is mostly due to the shunting of the cell. It is worth noting that, although the failure time is different for each individual cell, such a sudden shunting happened to all eight cells (Figure S1, Supporting Information), confirming this unexpected catastrophic failure is a general failure process for this type of cells.

## 2.2. Identifying the Shunting Position

To explore the location of the shunt in the PSCs, photoluminescence (PL) intensity mapping of a cell before and after aging were measured, and the results are shown in **Figure 2**a,b. The dashed and solid lines indicate the edge of ITO and Ag electrodes, respectively, and the overlap area is the active area of the cell. For the fresh device, the PL intensity over the Ag electrode area is lower than in other areas without top Ag electrode. However, it is homogenous over the entire area, indicating that the Ag electrode can effectively quench the perovskite film's fluorescence through effective hole injection from the perovskite to the Ag electrode. Interestingly, PL intensity increases slightly for the aged cell, especially at the Ag electrode edge of the active cell area. Time-resolved PL (TRPL) at different positions on the Ag electrode edge area was measured. The averaged fluorescence lifetime ($\tau$) gradually increases from 14.80 and 16.83 ns for the cell area (positions 1,2 in Figure 2b) to 23.19 and 28.24 ns for the area next to the Ag electrode edge (positions 3, 4 in Figure 2b), which is similar to the area without Ag electrode

(position 5, $\tau$ = 29.85 ns, see Table S2, Supporting Information for complete lifetime data), suggesting the changes of charge injection property at the perovskite/Spiro-OMeTAD/Ag interfaces on the edge of the electrode. To confirm whether shunting of the cell happened on the edge of the cell, we cut the two edges off with a knife and measured the current–voltage (J–V) characteristics again. As shown in Figure 2d, after cutting off the edge of the Ag electrode, the cell showed reasonably good photovoltaic behavior with recovered $V_{oc}$ of 1.07 V, FF of 0.63, and a high $J_{sc}$ over 20 mA cm$^{-2}$ (Table S3, Supporting Information, the effective cell area was estimated to be 0.05 cm$^2$), unambiguously confirming that shunting is localized on the edge of the cell. It worth noting that an increase of PL intensity was also measured in the center part of the cell (Figure 2b), indicating that interaction between perovskite film and the Spiro-OMeTAD/Ag metal happened as well in the center of the cell. This finding suggests that failure might happen in the center of the cell as well. However, the more significant edge corrosion (as seen from **Figure 3**a; Figure S3, Supporting Information) and no obvious morphology change of the perovskite film on the center part of the cell (Figure 3b) support that defects are mostly located on the Ag electrode edge.

In contrast, the cells kept in the glove box without light illumination showed almost no performance decay over the same aging time (Figure S2, Supporting Information), suggesting that light illumination is the most important driving force for shunting the cell. Figure S3, Supporting Information shows the appearance of the cells aged at different conditions. As seen

**ADVANCED
SCIENCE NEWS**
www.advancedsciencenews.com

**ADVANCED
FUNCTIONAL
MATERIALS**
www.afm-journal.de
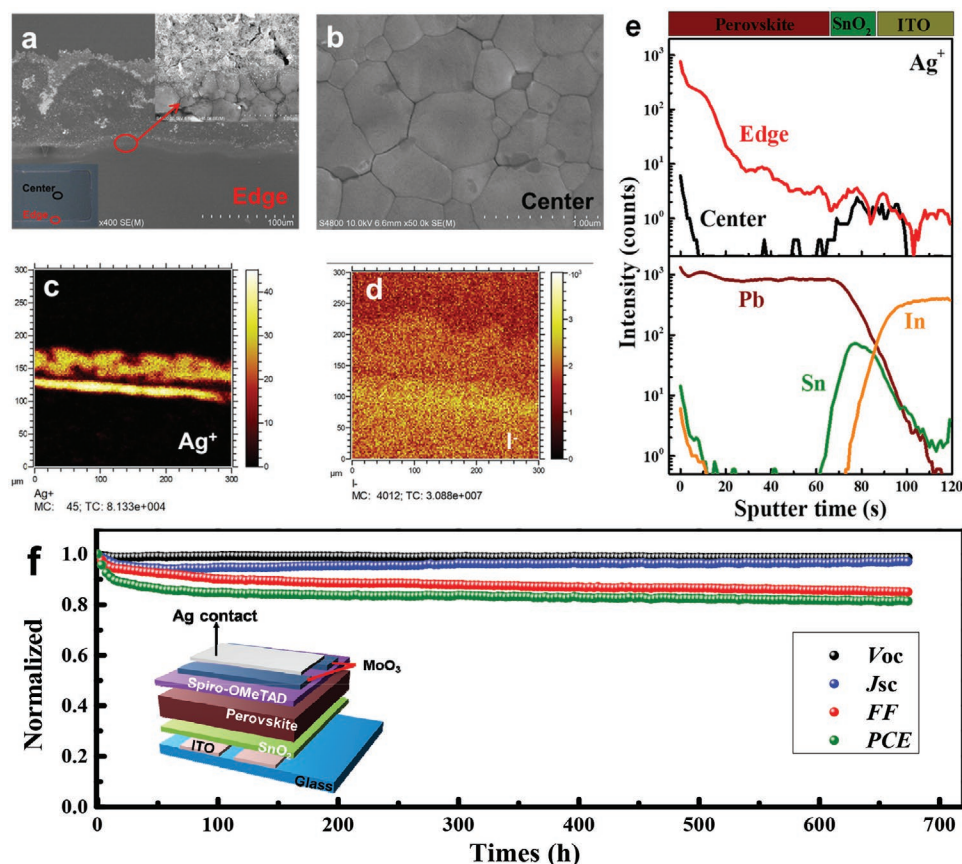
**Figure 3.** a,b) SEM images of the perovskite film after removing the Spiro-OMeTAD and Ag layers, and c,d) TOF-SIMS mapping of the perovskite surface on the Ag electrode edge; e) depth profiles of different Ag elements of the aged device after peeling off the Ag electrode and Spiro-OMeTAD layer; f) operational stability of solar cells under continuous illumination after protecting the edge of Ag electrode by $MoO_3$ layer.

there, the cells aged under light illumination showed a clear contour of the Ag electrode even after the removal of the Ag electrode and Spiro-OMeTAD layers. In contrast, the cell aged in the dark showed homogenous films over the entire area, indicating that light illumination is necessary for the unexpected sudden shunting of the cells.

Figure 3a,b shows the SEM images of the perovskite film at the edge and center area of the Ag electrode. Corrosion of the perovskite film under the Ag electrode edge can be clearly seen (Figure 3a). In contrast, the crystalline morphology of the perovskite film does not change too much in the center (Figure 3b), indicating the undesired decomposition of the perovskite film mostly on the Ag electrode edge. SIMS mapping (Figure 3c,d) showed high $Ag^+$ and $I^-$ concentrations of the decomposed perovskite film, suggesting that decomposition of the perovskite film is primarily due to the diffusion of silver atoms and the formation of AgI within the perovskite layer, similar to that reported in the literature.[27] The element depth distributions within the perovskite film were also characterized by time-of-flight secondary ion mass spectrometry (TOF-SIMS), and Figure 3d shows the results. As seen here, the $Ag^+$ ion profiles of the edge and the center area of the perovskite layer are different. At the edge area, shown as the red line, a high concentration of $Ag^+$ on the surface of the perovskite film was measured, corresponding well to the SIMS mapping

result (Figure 3c). Also, penetration of the $Ag^+$ through the whole perovskite film can be confirmed. However, almost no $Ag^+$ was detected in the perovskite layer at the center area, indicating inhomogeneous corrosion of the perovskite film by the Ag electrode.

To further confirm that $Ag^+$ ion migration at the edge of the Ag electrode is the main reason causing shunting, a 10 nm $MoO_3$ layer with a width of 3 mm was deposited between the Spiro-OMeTAD and Ag electrode on the edge while keeping no $MoO_3$ in the middle part of the cell (see Figure 3f for the device scheme). The J–V and external quantum efficiency (EQE) characterization of the champion devices are shown in Figure S4 and Table S4, Supporting Information, and the statistical performance data are compared to the standard cells (Figure S5, Supporting Information). After the insertion of the $MoO_3$ layer, the cells showed similar device efficiency as the standard cells (19.65% vs 19.52%). Then, these $MoO_3$ incorporated cells' operational stability was investigated under identical conditions for the reference cells. The results are shown in Figure 3f (see Figure S6, Supporting Information for the decay curves of five individual cells). Interestingly, the operational stability of PSCs was largely improved, and no shunting was measured for these cells even after aging for 670 h. More importantly, the optical (Figure S3i–l, Supporting Information) and SEM images (Figure S7, Supporting Information) of perovskite layer show

**ADVANCED**
**SCIENCE NEWS**
www.advancedsciencenews.com

**ADVANCED**
**FUNCTIONAL**
**MATERIALS**
www.afm-journal.de

that no obvious corrosion on the perovskite layer even after such a long-time aging, indicating that $MoO_3$ layer can prevent the corrosion of the Ag electrode over aging. Although we can't fully confirm that catastrophic failure will not happen over long aging times, the current experiment results clearly showed that $MoO_3$ layer can effectively suppress the short-term catastrophic failure of the n-i-p type cells.

### 2.3. Excluding the Influence of Bias, Water, and Oxygen

As mentioned above, a clear contour of the Ag electrode formed for the aged cell after removing the Spiro-OMeTAD and silver electrode (Figure S3, Supporting Information). Although all these cells were aged inside the glovebox with a low water and oxygen content (≤10 ppm), we cannot entirely exclude the oxidation of the Ag electrode during aging. To confirm whether water and/or oxygen is involved in the chemical corrosion of Ag electrode, we encapsulated the PSCs with EVA (ethylene vinyl acetate) and POE (polyolefin) sandwiched between two glass slides. The cells were aged under identical conditions. The results are shown in Figure S8, Supporting Information. As seen there, shunting was also found for the cell with complete encapsulation, proving that shunting of the cell should not be due to the diffusion of gas molecules through the edge but rather an intrinsic behavior of the cells.

Jeangros et al. reported the shunting of the p-i-n type PSCs under reverse bias (up to −2 V).[20] To further confirm whether the catastrophic failure of the cell is due to the bias effect during the $J$–$V$ sweeping, we tested the $J$–$V$ characteristics of the solar cells upon continuous $J$–$V$ sweeping from 1.2 to −0.05 V in the dark. The results of over 1400 scans (around 10 times of the $J$–$V$ sweeping for the cell starts catastrophic failure under operation) are shown in Figure S9, Supporting Information. No noticeable difference was observed in $J$–$V$ characteristics of the cell at different scanning time (Figure S9a, Supporting Information), and almost no increment of current density at a bias of 0.6 V (from 0.00521 to 0.00541 mA cm$^{-2}$, Figure S9b, Supporting Information), suggesting that no electric shunting was measured for this cell after multiple $J$–$V$ sweeping. Also, no noticeable loss of device performance was measured for the cell before and after multiple $J$–$V$ sweeping (Figure S9c, Supporting Information). These results indicate that the main driving force causing the catastrophic failure of the n-i-p type PSCs is the light illumination instead of the applied bias during the operational stability test.

### 2.4. Blocking the Diffusion of Reactive Iodide Species

Since oxygen or water is excluded from the oxidant causing the edge corrosion, the potential oxidants corroding the metal electrode can only come from the decomposition of perovskite film. It was reported that photo illumination on the perovskite film would lead to the formation of methanamine (MAI), HI, and $I_2$,[6] that could corrode the metal electrode. Abate et al. reported also that a thin $PbI_2$ layer on perovskite film could be transferred to black perovskite owing to the reaction of $PbI_2$ with released MAI.[43] Tarasov et al. recently reported that perovskite

thin-films could decompose by light illumination to form highly reactive methylammonium polyiodides $MAI_x$ ($x$ = 3, 5, and 7) melts,[25] which could be also the reactive species causing the corrosion of electrode. Since $MAI_x$ can react with $PbI_2$ to form the perovskite again (Equation 1),[44] $PbI_2$ should be the effective $MAI_x$ blocker that should increase device stability if $MAI_x$ is the main reactive species.

$$PbI_2 + MAI_x \rightarrow MAPbI_3 + I_{x-1} \qquad (1)$$

We therefore fabricated and tested PSCs with a thin $PbI_2$ layer inserted between the perovskite and Spiro-OMeTAD layers. **Figure 4**a,b shows the $J$–$V$ and EQE curves of the PSCs with $PbI_2$ layers (7 nm, see Figure 4b for the device structure). After the deposition of a thin $PbI_2$ layer on top of the perovskite film, the $V_{OC}$ of the cell increases slightly, which can be ascribed to the surface passivation effect of the $PbI_2$ layer.[45] However, both $J_{SC}$ and FF decrease yielding an overall performance decrease from 19.74% for the reference cell to 18.59% for the $PbI_2$ containing cell. The lower $J_{SC}$ and FF can be ascribed to the insulating nature of $PbI_2$.[46] In Figure 4c, we show the evolution of the photovoltaic performance of the cells under white light illumination. Although the time for the catastrophic failure of the reference cell is shorter than that of the cell shown in Figure 1 owing to the batch variation, all these reference cells showed catastrophic failure within 100 h (Figure S10, Supporting Information). As expected, the insertion of $PbI_2$ layer prolongs the mean failure time from 43 to 86 h. However, all these cells showed catastrophic failure under operation, suggesting that the $PbI_2$ cannot fully suppress the diffusion of reactive species. Since the reaction of $PbI_2$ with $MAI_x$ release $I_2$ as well, the current experiment results could not provide a confirmed conclusion on the reactive species for the corrosion of the Ag electrode. In combination with the results reported in literature,[6] photodecomposition of perovskite film forms volatile and reactive species, that will migrate through the Spiro-OMeTAD and reach the Ag electrode surface and consequently corrode the metal electrode. Nevertheless, prolonging the failure time after inserting a $PbI_2$ thin layer confirms that reactive species are coming from the decomposition of the perovskite layer under light illumination.

### 2.5. Morphology of the Ag Electrode

Since shunting of the cells mainly happens on the edge of the Ag electrodes, we checked for differences in the Ag electrode morphology. **Figure 5**a–c shows the surface morphology of the Ag electrode at different positions based on the Spiro-OMeTAD surface (see Figure S11, Supporting Information for the morphology changes cross the edge of the Ag electrode). It can be seen that the deposited Ag film is condensed and uniform in the central part of the electrode. In contrast, the Ag film at the edge comprises loose and unevenly distributed Ag cluster islands with a diameter of few nanometers. This is because Ag clusters on the edge are mainly formed from the diffused Ag atoms passing over the edge of the shadow mask. Similar morphology variation can also be seen in the Ag film deposited on $MoO_3$ surface (Figure 5d–f; Figures S11,S12, Supporting

**ADVANCED
SCIENCE NEWS**
www.advancedsciencenews.com

**ADVANCED
FUNCTIONAL
MATERIALS**
www.afm-journal.de
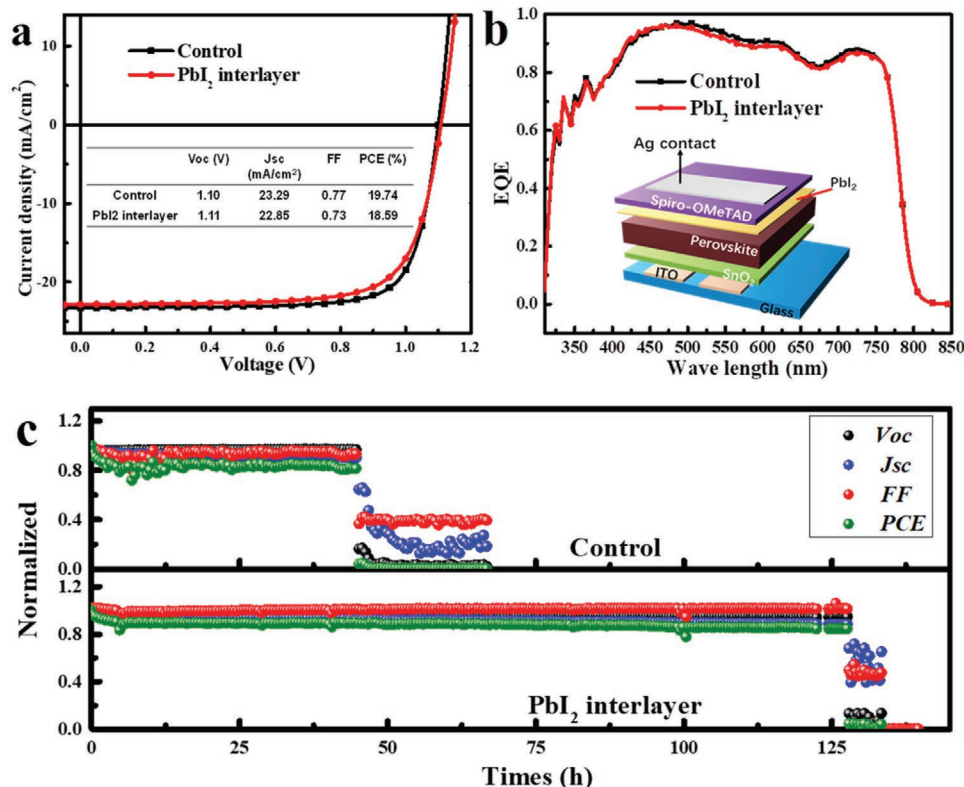
**Figure 4.** Solar cell performance of control and after PbI$_2$ modified a) J–V and b) EQE curves, inset shows the device structure of PbI$_2$ modified. c) Performance evolution of the cells under operation.

Information). However, the Ag film deposited on MoO$_3$ is more uniform with larger Ag clusters than that on Spiro-OMeTAD. It is known that MoO$_3$ could provide a good nucleation surface for the growth of Ag film, and the MoO$_3$ surface has a better wettability with Ag thin film.[47] The better compatibility between Ag on MoO$_3$ helps in forming more condense and uniformity Ag film, similar to the growth of other thin metal films reported in the literature.[48,49] Owing to the quantum size

effect, silver clusters with small diameters could be more easily be oxidized. Therefore, the loose structure of the Ag film on the Spiro-OMeTAD is one of the reasons for the poor stability in PSCs. Simultaneously, condensed Ag clusters on MoO$_3$ could improve the stability of the Ag electrode against corrosion.

The morphology differences on MoO$_3$ and Spiro-OMeTAD could then explain the variation of the failure time for the cells. In this work, both pre- and post-oxidation of the Spiro-OMeTAD
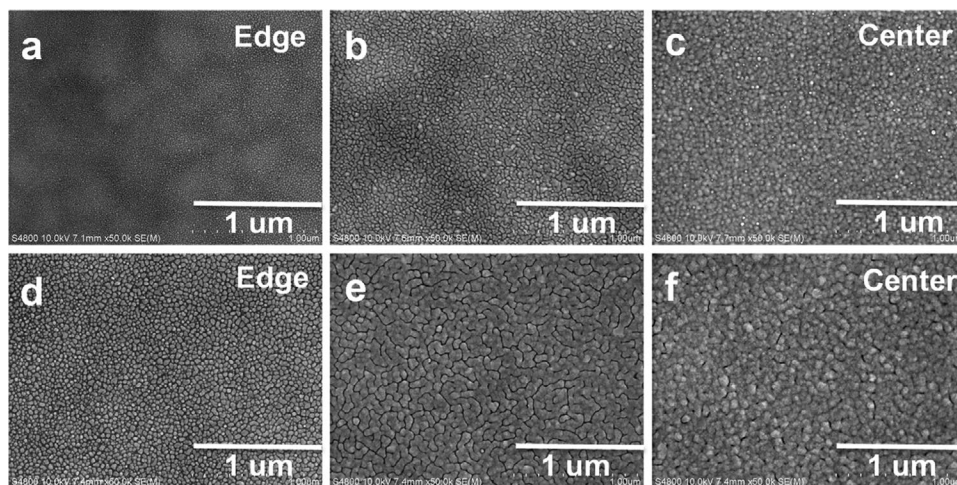


**Figure 5.** SEM image of freshly prepared Ag electrode from the edge to center deposited on a–c) Spiro-OMeTAD and d–f) MoO$_3$ substrate.

**ADVANCED
SCIENCE NEWS**
www.advancedsciencenews.com

**ADVANCED
FUNCTIONAL
MATERIALS**
www.afm-journal.de

layers were performed to improve the conductivity of the Spiro-OMeTAD layer and the consequent solar cell performance.[50] Although these cells were oxidized in air under similar conditions, the variation of device performance indicated that oxidization degree of the Spiro-OMeTAD films was not well controlled and the properties of Spiro-OMeTAD varied from batch to batch. In other words, the conductivity as well as the surface property of the Spiro-OMeTAD layer is different from each other after oxidation, which influences the silver electrode on it and leads to a large variation of the failure time during aging (Table S1, Figure S1, Supporting Information). A possible negative correlation between initial device performance and the failure time (Figure S13, Supporting Information) supports that oxidization process might also influence the catastrophic failure procedure as well.

### 2.6. Proposed Edge Corrosion Mechanism

Jeangros et al. reported the shunting of p-i-n type of PSCs under reverse bias (start at −2 V), which was ascribed to bias driven ion migration and segregation that leads to the formation of highly conductive regions through the cells.[23] In the current case, shunting of the n-i-p type of cells was driven by light illumination and it is accompanied with the severe corrosion of the metal electrode on the edge. The failure mechanism is slightly different from each other. The reactive species causing the corrosion of metal electrode are believed to be HI, $I_2$, and/or $MAI_x$, that originally come from the photodecomposition of the perovskite layer. Diffusion of these reactive iodinated species through the edge, along with the ease of oxidation of small and loose Ag cluster, corrosion of the metal electrode on the edge happens, which leads to the formation of $Ag^+$. The detection of high Ag concentration through the whole cell (Figure 3d) proves the migration of $Ag^+$, and the formation of highly conductive metal filament is supposed to be the reason for the shunting, which was found also in different electronic devices.[51] The proposed mechanism is then shown in **Figure 6**. After a thin $MoO_3$ or $PbI_2$ interface layer is introduced on the perovskite surface, the migration of iodide species is inhibited, so the corrosion rate of the Ag electrode slows down, and the stability is improved. For the $MoO_3$-containing cell, on the other hand, the deposited Ag film is denser with larger clusters, which is more difficult to be oxidized and therefore enhances the long-term stability of the cells.

### 2.7. Stabilization Effects of the $MoO_3$ Interlayer: More than Physical Blocking

As shown above, insertion of a thin $PbI_2$ (7 nm) or $MoO_3$ (10 nm) can improve the device stability. Although these two layers' thicknesses are quite similar, the $MoO_3$ layer can significantly improve the stability with no catastrophic failure over 600 h, while $PbI_2$ only prolongs the time before the catastrophic failure. This indicates the stability improvement of $MoO_3$ must be more than a simple physical blocking effect. The energy band alignment of the $MoO_3$-free and $MoO_3$-containing cells are then analyzed and shown in **Figure 7**, where the energy level values of perovskite,[52] Spiro-OMeTAD,[39] and $MoO_3$[53] are taken from the literature. As seen from Figure 7a, for the $MoO_3$-free cell, the transport of photoexcited holes via the valence band of Spiro-OMeTAD toward the Ag electrode. It facilitates the oxidation of Ag and the subsequent migration of $Ag^+$ ions. In contrast, inserting a $MoO_3$ layer leads to interface recombination between photoexcited holes at the ohmic contact formed between $Ag/MoO_3$ and Spiro-OMeTAD (Figure 7b). As a result, the holes created within the perovskite layer are well separated from the Ag electrode, improving the stability of the $MoO_3$ based cell. Hence, our results suggest that our strategy to reduce the accumulation of holes at the hole transporting layer/Ag interface is proposed as an effective way to improve the stability of n-i-p type PSCs.

## 3. Conclusion

In summary, we report the undesired catastrophic shunting of the n-i-p type PSCs under simulated operational conditions. The shunting position was confirmed to be at the edge of the Ag electrode by PL intensity and lifetime results and the recovery of the cell performance by cutting the edge off. SEM images and TOF-SIMS analyses gave direct evidence of the $Ag^+$ migration at the edge of the device. Suppression of the shunting was successfully achieved by inserting a thin $MoO_3$ layer at the Ag edge or inserting a thin $PbI_2$ layer between the perovskite and Spiro-OMeTAD layers. The SEM images of the Ag morphology results revealed that the size of Ag clusters is smaller and looser for the Ag electrode edge on top of Spiro-OMeTAD. In contrast, larger and more condensed Ag clusters were found for the central part of the Ag electrode on top of Spiro-OMeTAD and the entire Ag film on $MoO_3$. The latter
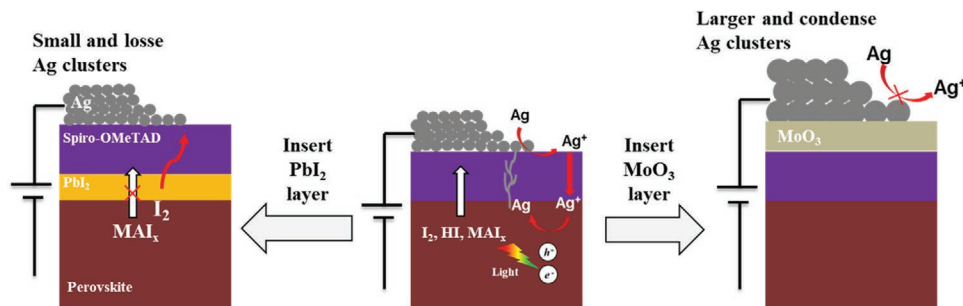


**Figure 6.** The proposed Ag electrode induced degradation mechanism of n-i-p type PSCs.
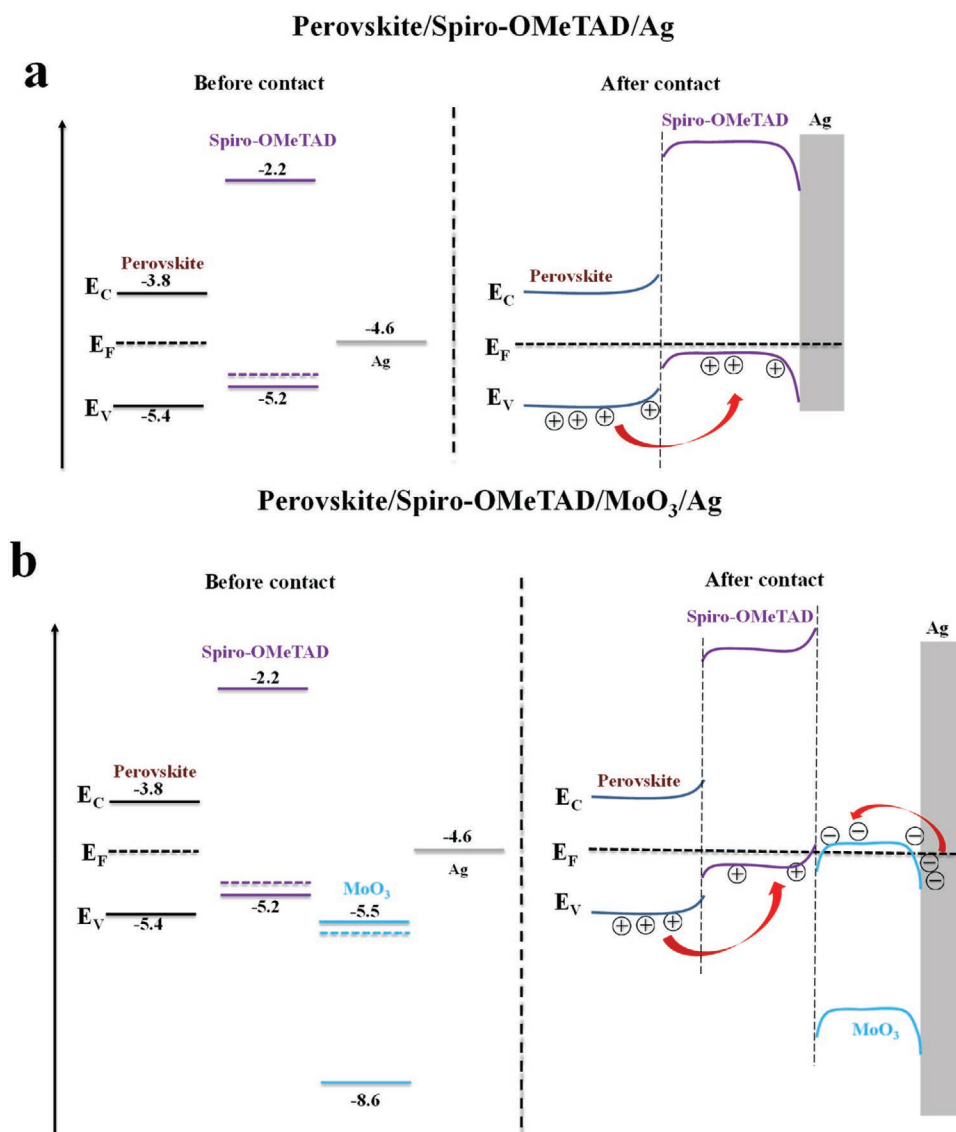
**Figure 7.** The schematic description of the interface band bending of a) perovskite/Spiro-OMeTAD/Ag and b) perovskite/Spiro-OMeTAD/MoO$_3$/Ag, before and after contact.

phenomenon can be ascribed to better compatibility for Ag film growth on top of MoO$_3$. The failure mechanism was proposed based on these experimental results. The formation of reactive polyiodine melts under light illumination, diffusing and reacting with small Ag clusters and forming mobile Ag$^+$ ions. The migration of Ag$^+$ ions through the Spiro-OMeTAD and perovskite layer leads to conducting Ag filaments, which causes the irreversible shunting of the cells. In addition, the improved band alignment of the MoO$_3$-containing cells can successfully separate the holes from the Spiro-OMeTAD/Ag interface, which is suggested to be an effective way to suppress the catastrophic failure of n-i-p type PSCs.

## 4. Experimental Section

*Materials*: The SnO$_2$ colloid solution was purchased from Alfa Aesar (tin (IV) oxide, 15 wt% in H$_2$O colloidal dispersion). PbI$_2$, PbBr$_2$, CsI,

formamidinium iodide (FAI), methylammonium bromide (MABr), lithium bis(trifluoromethanesulphony)imide (LiTFSI), pyridine,4-(1,1-dimethylethyl)- (t-BP), and Spiro-OMeTAD were purchased from Xi'an Polymer Light Technology Corp', dimethylformamide (DMF, purity > 99%), dimethyl sulfoxide (DMSO, purity > 99%), and chlorobenzene (CB, purity > 99%) were purchased from J&K scientific. All materials were used directly.

*Instruments and Characterization*: The current density-voltage (J–V) characters of solar cells were measured with a Keithley 2400 source meter in N$_2$ glove box under a simulated sun AM 1.5 G (Newport VeraSol- 2 LED Class AAA Solar Simulator). The TOF-SIMS (5–100) was measured with the pulsed primary ions from a Cs$^+$ (2 keV) liquid-metal ion gun for sputtering and a Bi$^+$ pulsed primary ion beam for analysis (30 keV). Photofluorescence imaging of solar cells was conducted under laser radiation with wavelength of 532 nm. SEM images were gained by a field-emission scanning electron microscope (S-4800) under an accelerating voltage of 10 kV. The X-ray and ultraviolet photoelectron spectroscopy measurements were conducted at a PHI 5000 VersaprobeII system. Operational stability measurement was conducted at D&R Instruments (PVLT-G8001M-256H).

*Preparation of the Perovskite Precursor and Spiro-OMeTAD Solution*: The $SnO_2$ colloid solution (15 wt%) was diluted using deionized water to the concentration of 3 wt%. This solution was stirred at room temperature for 2 h. The $K_{0.035}Cs_{0.05}(FA_{0.85}MA_{0.15})_{0.95}Pb(I_{0.85}Br_{0.15})_3$ precursor solution was prepared by dissolving $PbI_2$ (548.6 mg), $PbBr_2$ (77.07 mg), FAI (190.12 mg), and MABr (21.84 mg) in a mixture solvent of DMF/DMSO (1 mL, 4:1 v/v). Then, 34 μL CsI (2 м in DMSO) and 25 μL KI (2 M in DMSO) was added to mixed perovskite solution, stirring overnight at room temperature. The Spiro-OMeTAD solution was prepared by dissolving 72.3 mg Spiro-OMeTAD into 1 mL chlorobenzene followed by the addition of 17.5 μL Li-TFSI (520 mg mL$^{-1}$ in acetonitrile) and 29 μL t-BP, this solution was stirred overnight at room temperature.

*Solar Cell Fabrication*: ITO glass was cleaned by ultrasonic cleaning through detergent, pure water, acetone, and isopropanol for 30 min, respectively. Before using, the ITO substrate was dried by $N_2$ gas flow, and cleaned by UV Ozone for 30 min. Then the substrate was spin-coated with a thin layer of $SnO_2$ nanoparticle from the $SnO_2$ colloid solution at 3000 rpm for 30 s, and annealed in ambient air at 150 °C for 30 min. The Perovskite precursor solution was spin-coated on the $SnO_2$ substrate. The spin-coated process was divided by a consecutive two-step process, the spin rate of the first step was 2000 rpm for 10 s with accelerated speed of 500 rpm, and the spin rate of the second step was 6000 rpm for 20 s with accelerated speed of 1000 rpm. During the second step end of 10 s, 400 μL of ethyl acetate was drop-coated to treat the perovskite films, and then the perovskite films were annealed at 120 °C for 45 min in a glovebox. After cooling down to room temperature, the spiro-OMeTAD solution was coated on perovskite films at 3000 rpm for 30 s with accelerated speed of 3000 rpm. Then, the Spiro-OMeTAD layer was fully oxidized in air with humidity of 30% overnight.

For the solar cell without $MoO_3$: 100 nm thick Ag was deposited on the Spiro-OMeTAD by thermal evaporation with rate of 0.8 Å s$^{-1}$. Then, oxidized the full cells in air for 5 h, with a control humidity of 30%.

For the solar cell with $MoO_3$: 10 nm thick $MoO_3$ was deposited on the Spiro-OMeTAD with rate of 0.2 Å s$^{-1}$, then 100 nm thick Ag was deposited.

For the solar cell with $PbI_2$: 7 nm thick $PbI_2$ was deposited on the Perovskite layer with rate of 0.1 Å s$^{-1}$. Then finish the device with Spiro-OMeTAD and Ag electrode.

*Encapsulation of Solar Cells*: The solar cell was encapsulated by EVA/POE and covered with slide glass. The melting condition of EVA was 90 °C, 3 min, and the pressing time was 7 s. The melting condition of POE was 140 °C, 3 min, and the pressing time was 7 s. The encapsulation process was completed in $N_2$ glove box.

*Operational Stability Test*: Operational stability of the cells was performed on a multi-channel solar cell performance decay testing system ((PVLT-G8001M, Suzhou D&R Instruments Co. Ltd.) inside a $N_2$-filled glove box ($H_2O$ < 10 ppm, $O_2$ < 10 ppm), and the cells were illuminated with a white LED light (D&R Light, L-W5300KA-150, Suzhou D&R Instruments Co. Ltd. see Figure S14, Supporting Information for the light spectrum) at a simulated one sun intensity (the initial short current equals to the $J_{SC}$ measured under standard condition). The cell's performance was measured by I–V sweeping from 1.2 to −0.05 V, with a step of 0.01 V. The temperature was measured from time to time and it was around 40–50 °C.

## Supporting Information

Supporting Information is available from the Wiley Online Library or from the author.

## Conflict of Interest

The authors declare no conflict of interest.

## Data Availability Statement

The data that supports the findings of this study are available in the supplementary material of this article.

[1] Q. Jiang, Y. Zhao, X. Zhang, X. Yang, Y. Chen, Z. Chu, Q. Ye, X. Li, Z. Yin, J. You, *Nat. Photonics* **2019**, *13*, 460.

[2] T. A. S. Doherty, A. J. Winchester, S. Macpherson, D. N. Johnstone, V. Pareek, E. M. Tennyson, S. Kosar, F. U. Kosasih, M. Anaya, M. Abdi-Jalebi, Z. Andaji-Garmaroudi, E. L. Wong, J. Madéo, Y.-H. Chiang, J.-S. Park, Y.-K. Jung, C. E. Petoukhoff, G. Divitini, M. K. L. Man, C. Ducati, A. Walsh, P. A. Midgley, K. M. Dani, S. D. Stranks, *Nature* **2020**, *580*, 360.

[3] J. Peng, D. Walter, Y. Ren, M. Tebyetekerwa, Y. Wu, T. Duong, Q. Lin, J. Li, T. Lu, M. A. Mahmud, O. L. C. Lem, S. Zhao, W. Liu, Y. Liu, H. Shen, F. K. LiLi, H. T. Nguyen, D.-Y. Choi, K. J. Weber, K. R. Catchpole, T. P. White, *Science* **2021**, *371*, 390.

[4] A. Kojima, K. Teshima, Y. Shirai, T. Miyasaka, *J. Am. Chem. Soc.* **2009**, *131*, 6050.

[5] Best Research-Cell Efficiencies: Emerging Photovoltaics, https://www.nrel.gov/pv/assets/pdfs/cell-pv-eff-emergingpv.202001042.pdf (accessed: March 2021).

[6] C. C. Boyd, R. Cheacharoen, T. Leijtens, M. D. McGehee, *Chem. Rev.* **2019**, *119*, 3418.

[7] S. Zhang, Z. Liu, W. Zhang, Z. Jiang, W. Chen, R. Chen, Y. Huang, Z. Yang, Y. Zhang, L. Han, W. Chen, *Adv. Energy Mater.* **2020**, *10*, 2001610.

[8] Y. Jiang, S.-C. Yang, Q. Jeangros, S. Pisoni, T. Moser, S. Buecheler, A. N. Tiwari, F. Fu, *Joule* **2020**, *4*, 1087.

[9] T. H. Schloemer, J. A. Raiford, T. S. Gehan, T. Moot, S. Nanayakkara, S. P. Harvey, R. C. Bramante, S. Dunfield, A. E. Louks, A. E. Maughan, L. Bliss, M. D. McGehee, M. F. A. M. van Hest, M. O. Reese, S. F. Bent, J. J. Berry, J. M. Luther, A. Sellinger, *ACS Energy Lett.* **2020**, *5*, 2349.

[10] Y. Cheng, L. Ding, *Energy Environ. Sci.* **2021**, *14*, 3233.

[11] J. Ali, Y. Li, P. Gao, T. Hao, J. Song, Q. Zhang, L. Zhu, J. Wang, W. Feng, H. Hud, F. Liu, *Nanoscale* **2020**, *12*, 5719.

[12] X. Li, S. Fu, S. Liu, Y. Wu, W. Zhang, W. Song, J. Fang, *Nano Energy* **2019**, *64*, 103962.

[13] J. S. Yun, J. Kim, T. Young, R. J. Patterson, D. Kim, J. Seidel, S. Lim, M. A. Green, S. Huang, A. Ho-Baillie, *Adv. Funct. Mater.* **2018**, *28*, 1705363.

[14] B. Kim, M. Kim, J. H. Lee, S. I. Seok, *Adv. Sci.* **2020**, *7*, 1901840.

[15] Z. Yang, J. Dou, S. Kou, J. Dang, Y. Ji, G. Yang, W.-Q. Wu, D.-B. Kuang, M. Wang, *Adv. Funct. Mater.* **2020**, *30*, 1910710.

[16] L. Shi, M. P. Bucknall, T. L. Young, M. Zhang, L. Hu, J. Bing, D. S. Lee, J. Kim, T. Wu, N. Takamure, D. R. McKenzie, S. Huang, M. A. Green, A. W. Y. Ho-Baillie, *Science* **2020**, *368*, 1328.

[17] Y. Cheng, Q.-D. Yang, L. Ding, *Sci. Bull.* **2021**, *66*, 100.

[18] Y. Wang, Z. Zhang, Y. Lan, Q. Song, M. Li, Y. Song, *Angew. Chem., Int. Ed.* **2021**, *60*, 8673.

[19] M. V. Khenkin, K. M. A., E. A. Katz, I. Visoly-Fisher, *Energy Environ. Sci.* **2019**, *12*, 550.

[20] R. A. Z. Razera, M. Dussouillez, F. Sahli, D. A. Jacobs, F. Fu, P. Fiala, T. C. J. Yang, L. Ding, A. Walter, A. F. Feil, H. I. Boudinov, S. Nicolay, C. Ballif, Q. Jeangros, *J. Mater. Chem. A* **2020**, *8*, 242.

[21] E. T. Hoke, D. J. Slotcavage, E. R. Dohner, A. R. Bowring, H. I. Karunadasa, M. D. McGehee, *Chem. Sci.* **2015**, *6*, 613.

[22] D. W. deQuilettes, W. Zhang, V. M. Burlakov, D. J. Graham, T. Leijtens, A. Osherov, V. Bulovic, H. J. Snaith, D. S. Ginger, S. D. Stranks, *Nat. Commun.* **2016**, *7*, 11683.

[23] W. Li, W. Zhang, S. V. Reenen, R. J. Sutton, J. Fan, A. A. Haghighirad, M. B. Johnston, L. Wang, H. J. Snaith, *Energy Environ. Sci.* **2016**, *9*, 490.

[24] J. A. Christians, P. Schulz, J. S. Tinkham, T. H. Schloemer, S. P. Harvey, B. J. T. de Villers, A. Sellinger, J. J. Berry, J. M. Luther, *Nat. Energy* **2018**, *3*, 68.

[25] N. N. Shlenskaya, N. A. Belich, M. Gr¨atzel, E. A. Goodilin, A. B. Tarasov, *J. Mater. Chem. A* **2018**, *6*, 1780.

[26] C. Besleaga, L. E. Abramiuc, V. Stancu, A. G. Tomulescu, M. Sima, L. Trinca, N. Plugaru, L. Pintilie, G. A. Nemnes, M. Iliescu, H. G. Svavarsson, A. Manolescu, I. Pintilie, *J. Phys. Chem. Lett.* **2016**, *7*, 5168.

[27] S. Svanström, T. J. Jacobsson, G. Boschloo, E. M. J. Johansson, H. Rensmo, U. B. Cappel, *ACS Appl. Mater. Interfaces* **2020**, *12*, 7212.

[28] J. Li, Q. Dong, N. Li, L. Wang, *Adv. Energy Mater.* **2017**, *7*, 1602922.

[29] Z. Huang, A. H. Proppe, H. Tan, M. I. Saidaminov, F. Tan, A. Mei, C.-S. Tan, M. Wei, Y. Hou, H. Han, S. O. Kelley, E. H. Sargent, *ACS Energy Lett.* **2019**, *4*, 1521.

[30] M. Li, W.-W. Zuo, Q. Wang, K.-L. Wang, M.-P. Zhuo, H. Köbler, C. E. Halbig, S. Eigler, Y.-G. Yang, X.-Y. Gao, Z.-K. Wang, Y. Li, A. Abate, *Adv. Energy Mater.* **2019**, *10*, 1902653.

[31] J. Zhang, S. Hou, R. Li, B. Chen, F. Hou, X. Cui, J. Liu, Q. Wang, P. Wang, D. Zhang, Y. Zhao, X. Zhang, *J. Semicond.* **2020**, *41*, 052202.

[32] E. Bi, H. Chen, F. Xie, Y. Wu, W. Chen, Y. Su, A. Islam, M. Grätzel, X. Yang, L. Han, *Nat. Commun.* **2017**, *8*, 15330.

[33] X. Li, W. Zhang, Y.-C. Wang, W. Zhang, H.-Q. Wang, J. Fang, *Nat. Commun.* **2018**, *9*, 3806.

[34] M. Ohring, L. Kasprzak, in *Reliability and Failure of Electronic Materials and Devices*, Academic Press, Cambridge **2015**, p. 181.

[35] W. Luo, Y. S. Khoo, P. Hacke, V. Naumann, D. Lausch, S. P. Harvey, J. P. Singh, J. Chai, Y. Wang, A. G. Aberle, S. Ramakrishna, *Energy Environ. Sci.* **2017**, *10*, 43.

[36] M. B. Hartenstein, W. Nemeth, V. LaSalvia, S. Harvey, H. Guthrey, S. Theingi, M. Page, D. L. Young, P. Stradins, S. Agarwal, *IEEE J. Photovoltaics* **2020**, *10*, 1574.

[37] T. Bu, X. Liu, Y. Zhou, J. Yi, X. Huang, L. Luo, J. Xiao, Z. Ku, Y. Peng, F. Huang, Y.-B. Cheng, J. Zhong, *Energy Environ. Sci.* **2017**, *10*, 2509.

[38] A. Abate, T. Leijtens, S. Pathak, J. l. Teuscher, R. Avolio, M. E. Errico, J. Kirkpatrik, J. M. Ball, P. Docampo, I. McPhersonc, H. J. Snaith, *Phys. Chem. Chem. Phys.* **2013**, *15*, 2572.

[39] Z. Hawash, L. K. Ono, Y. Qi, *Adv. Mater. Interfaces* **2018**, *5*, 1700623.

[40] L. Wang, G. Wang, Z. Yan, J. Qiu, C. Jia, W. Zhang, C. Zhen, C. Xu, K. Tai, X. Jiang, S. Yang, *Sol. RRL* **2020**, *4*, 2000098.

[41] F. Zheng, W. Chen, T. Bu, K. P. Ghiggino, F. Huang, Y. Cheng, P. Tapping, T. W. Kee, B. Jia, X. Wen, *Adv. Energy Mater.* **2019**, *9*, 1901016.

[42] IEC TS 62876-2-1:2018, https://webstore.iec.ch/publication/26699 (accessed: August 2018)

[43] K. Domanski, B. Roose, T. Matsui, M. Saliba, S.-H. Turren-Cruz, J.-P. Correa-Baena, C. R. Carmona, G. Richardson, J. M. Foster, F. D. Angelis, J. M. Ball, A. Petrozza, N. Mine, M. K. Nazeeruddin, W. Tress, M. Grätzel, U. Steiner, A. Hagfeldtd, A. Abate, *Energy Environ. Sci.* **2017**, *10*, 604.

[44] A. A. Petrov, N. A. Belich, A. Y. Grishko, N. M. Stepanov, S. G. Dorofeev, E. G. Maksimov, A. V. Shevelkov, S. M. Zakeeruddin, M. Graetzel, A. B. Tarasov, E. A. Goodilin, *Mater. Horiz.* **2017**, *4*, 625.

[45] Q. Chen, H. Zhou, T.-B. Song, S. Luo, Z. Hong, H.-S. Duan, L. Dou, Y. Liu, Y. Yang, *Nano Lett.* **2014**, *14*, 4158.

[46] G. Tumen-Ulzii, C. Qin, D. Klotz, M. R. Leyden, P. Wang, M. Auffray, T. Fujihara, T. Matsushima, J.-W. Lee, S.-J. Lee, Y. Yang, C. Adachi, *Adv. Mater.* **2020**, *32*, 1905035.

[47] C. Zhang, C. Ji, Y.-B. Park, L. J. Guo, *Adv. Opt. Mater.* **2020**, *9*, 2001298.

[48] P.-C. Kao, C.-J. Hsieh, Z.-H. Chen, S.-H. Chen, *Sol. Energy Mater. Sol. Cells* **2018**, *186*, 131.

[49] Y.-G. Bi, Y.-F. Liu, X.-L. Zhang, D. Yin, W.-Q. Wang, J. Feng, H.-B. Sun, *Adv. Opt. Mater.* **2019**, *7*, 1800778.

[50] C. Ding, R. Huang, C. Ahl¨ang, J. Lin, L. Zhang, D. Zhang, Q. Luo, F. Li, R. Österbacka, C.-Q. Ma, *J. Mater. Chem. A* **2021**, *9*, 7575.

[51] S. Lee, H. Kim, D. H. Kim, W. B. Kim, J. M. Lee, J. Choi, H. Shin, G. S. Han, H. W. Jang, H. S. Jung, *ACS Appl. Mater. Interfaces* **2020**, *12*, 17039.

[52] C. Altinkaya, E. Aydin, E. Ugur, F. H. Isikgor, A. S. Subbiah, M. D. Bastiani, J. Liu, A. Babayigit, T. G. Allen, F. Laquai, A. Yildiz, S. D. Wolf, *Adv. Mater.* **2021**, *33*, 2005504.

[53] J. Meyer, A. Kahn, *J. Photonics Energy* **2011**, *1*, 011109.